




Sound speed measurements in silver shock compressed to 300 GPa: Solid-state transition, melting, and liquid-state response

M. K. Wallace ¹, J. M. Winey ^{1,*} and Y. M. Gupta ^{1,2}

¹*Institute for Shock Physics, Washington State University, Pullman, Washington 99164-2816, USA*

²*Department of Physics and Astronomy, Washington State University, Pullman, Washington 99164-2814, USA*



(Received 10 November 2021; revised 6 December 2021; accepted 9 December 2021; published 20 December 2021)

To gain insight into the thermodynamic response of shock-compressed Ag states corresponding to the face-centered-cubic (fcc) to body-centered-cubic (bcc) transformation and melting observed using *in situ* x-ray diffraction (XRD) measurements [Phys. Rev. Lett. **124**, 235701 (2020)], we present longitudinal sound speed results and their analysis in Ag at peak stresses ranging from 60 to 300 GPa. The measured sound speeds increased linearly with density compression to 171 GPa, showing that the sound speeds (and longitudinal moduli) in the fcc and bcc phases are very similar. Between 171 and 218 GPa, the sound speed dropped significantly, consistent with the melting reported using XRD measurements in shock-compressed Ag. From 218 to 300 GPa, the increasing sound speeds and Hugoniot states provide a determination of the liquid phase Ag response. In particular, determination of the Grüneisen parameter (Γ) showed that the density–Grüneisen parameter product ($\rho\Gamma$) for liquid Ag is constant, but differs significantly from that for solid Ag at ambient conditions. Thus, the Mie–Grüneisen equation of state can be used to describe the Hugoniot and off-Hugoniot response of liquid Ag.

DOI: [10.1103/PhysRevB.104.214106](https://doi.org/10.1103/PhysRevB.104.214106)

I. INTRODUCTION

Due to their unique physical and chemical attributes, noble metals have been of long-standing scientific and technological interest. In particular, noble metals have been used extensively as pressure markers in scientific studies at high pressures [1–8] and as impedance-matching standards for shock compression studies [2,7,9–11]. Their use in static and dynamic compression studies was based, in part, on the observed stability of their ambient face-centered-cubic (fcc) structure under static compression [1,3–6,8] and the assumed stability of the fcc phase under shock compression up to the melting stress [2,7,12,13].

Recently, *in situ* x-ray diffraction (XRD) measurements in laser-shock experiments revealed that the ambient fcc structure is not stable for shock-compressed gold, silver, and copper, but instead transforms to the body-centered-cubic (bcc) structure at stresses ranging from ~ 150 to ~ 180 GPa [14–17]. XRD data showing the onset of melting at higher stresses were also reported for all three metals [14–17]. Prior to these XRD studies, the melting curves for noble metals under static compression were reported only up to 8 GPa for Ag and Au [18,19] and to 100 GPa for Cu [18–21], and measured melting stresses for noble metals under shock compression were reported only for Cu [22]. Although many previous equation of state developments for noble metals have been reported [1,2,7,12,13], the recent XRD results have stimulated renewed interest in theoretical determination of phase diagrams for noble metals [23,24].

Complementary to XRD measurements, sound speed measurements have been shown to provide important insight into phase transformations in metals shock compressed to high stresses [22,25–32]. Furthermore, sound speed results provide important thermodynamic constraints to facilitate development of the equations of state (EOS) for metals at high stresses [22,26]. Sound speeds are particularly important for metals shock compressed into the liquid phase, where XRD measurements provide little insight and experimental data to guide EOS developments are often lacking. For noble metals under shock compression, sound speeds have been reported only for copper [22,30].

Compared to other noble metals, the shock compression response of silver has received significantly less attention. Using impedance matching, two studies have reported Hugoniot states for Ag at high stresses [10,33]. However, the results are somewhat sparse and the measured states from the two reports differ at stresses above 50 GPa. Recently, we reported on wave profile measurements for Ag shock compressed to 300 GPa [34]. Hugoniot states determined from the wave profiles were intermediate between those reported from the two previous studies [10,33] and provided a more accurate determination of the Ag Hugoniot curve. In addition, small features appearing in the measured wave profiles suggested the onset of melting between 171 and 187 GPa, consistent with the XRD results [16]. Despite the accurate determination of the Ag Hugoniot [34], there were no discernible features corresponding to the fcc-bcc transition or the solid-liquid transition. Over the entire stress range (30–300 GPa) examined, a single Hugoniot curve provided an excellent fit to the measured results.

To gain insight into the shock-compressed Ag states, we present here longitudinal sound speed measurements and their analysis in Ag shock compressed to 300 GPa. Specifically,

*mwiney@wsu.edu

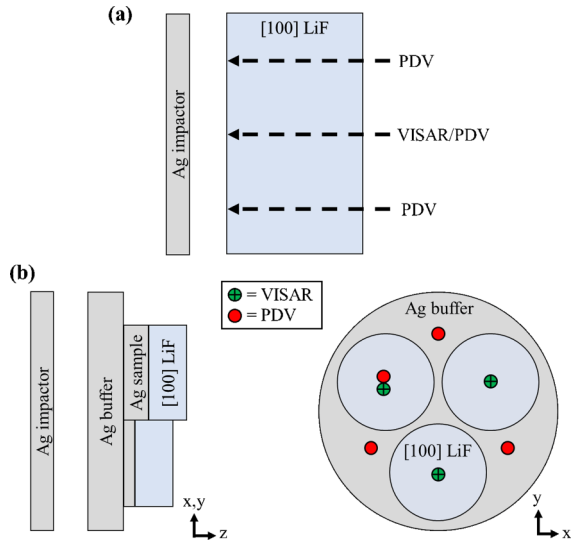


FIG. 1. Experimental configurations for (a) front surface impact experiments and (b) release wave overtake experiments to measure wave profiles and sound speeds in shock-compressed Ag.

the present work was motivated by the following objectives: (1) to gain insight into the fcc-bcc transformation and melting in shock-compressed Ag reported previously based on XRD [16] measurements, and (2) to gain insight into the thermodynamic response of the Ag liquid state achieved under shock compression.

The present paper is organized as follows. The experimental methods are presented in Sec. II. The experimental results, including the measured wave profiles, are presented in Sec. III. The results are analyzed and discussed in relation to the previous XRD [16] and wave profile [34] results in Sec. IV. The main findings of this work are summarized in Sec. V.

II. EXPERIMENTAL METHODS

The silver (99.95+% purity) samples used in this study were obtained as polycrystalline rods from Goodfellow. The average ambient density, determined using the Archimedeian method, was 10.50 ± 0.01 g/cc. Average longitudinal and shear sound speeds, measured using the pulse-echo technique, were 3.72 ± 0.01 and 1.63 ± 0.02 mm/ μ s, respectively. These results are consistent with published values for silver [10,35,36].

Plate impact experiments were carried out using our two-stage light gas gun facility. As shown in Fig. 1, two experimental configurations were used in the present work to access a large range of shock stresses (60–300 GPa). We note that, in the first configuration, the impact stresses are limited by the maximum projectile velocity achievable (~ 7.6 km/s) and the window Hugoniot. For both configurations, the impactor and target dimensions were chosen such that the Ag sample remained in a uniaxial strain state for the duration of the data acquisition.

For the first configuration, shown in Fig. 1(a), a front surface impact design was used in which the Ag sample—mounted on the projectile—was impacted directly onto the

[100] lithium fluoride (LiF) window. A thin aluminum mirror was vapor deposited onto the impact side of the LiF window. Particle velocity histories were measured at the impactor/window interface using two types of laser interferometry—VISAR (Velocity Interferometer System for Any Reflector [37]) and PDV (Photon Doppler Velocimetry [38]). As shown in Fig. 1(a), VISAR and PDV were used for the center probe to measure the wave profile at the impactor/window interface. The three outer PDV probes were positioned at 120° azimuthal intervals to determine the impact tilt.

For the second configuration, shown in Fig. 1(b), the release wave overtake approach [25,26,39] was used. In this approach, which permits higher stress measurements, Ag samples—each having a different thickness and backed by a LiF window—were bonded to the back side of a Ag buffer using a thin (~ 1 μ m) epoxy bond. The resulting Ag thicknesses (nominally between ~ 0.8 and ~ 1.4 mm), as measured from the impact surface, are labeled as I, II, and III in Table I. The target assembly was impacted with an Ag flyer. Particle velocity histories were measured at the Ag/LiF interfaces and at the Ag buffer free surface using laser interferometry. For the thickest Ag samples, both VISAR and PDV were used to measure the wave profiles at the sample/window interface. For the thinner Ag samples, only VISAR was used. The three PDV probes on the back of the Ag buffer were positioned at 120° azimuthal intervals to determine the tilt and arrival time of the shock wave front.

A total of ten experiments were conducted in this work; the relevant experimental parameters are listed in Table I.

III. RESULTS

For both the front surface impact experiments and the release wave overtake experiments, wave profiles measured at the Ag/LiF interface were corrected for shock-induced changes in the [100] LiF refractive index [40]. A dual velocity-per-fringe configuration was used for the VISAR measurements to ensure unambiguous particle velocity determination. Measured shock velocities, peak Ag/LiF interface velocities, and corresponding in-material states are listed in Table II. The analytic procedure used to obtain the in-material states is described in Sec. IV.

Figure 2 shows the wave profiles measured in the front surface impact experiments (experiments 1, 2, 4–6); the time axis is normalized by the Ag impactor thickness and impact occurs at time zero. The wave profiles measured using the VISAR and PDV are in excellent agreement with each other and show an abrupt jump to the peak interface velocity. The velocity then remains constant until the arrival of the release wave from the back of the impactor (marked with an arrow in Fig. 2). The measured time interval between impact and release wave arrival (Δt)—used to determine the longitudinal sound speed in the shocked state—is listed in Table III.

Figure 3(a) shows the wave profiles measured for each Ag thickness (labeled I, II, and III) in a representative release wave overtake experiment (experiment 10); the wave profiles measured in experiments 3 and 7–9 are very similar. The wave profiles measured using the VISAR and PDV probes are in excellent agreement. Time zero corresponds to the shock

TABLE I. Experimental parameters.

Experiment No.	Experimental configuration ^a	Ag impactor thickness, h_i (mm)	Impactor velocity, V_p (mm/ μ s)	Ag target thicknesses (mm) I/II/III ^{b,c}
1 (20-2SH52)	FI	0.357 ± 0.002	3.822 ± 0.005	
2 (20-2SH05)	FI	1.002 ± 0.002	5.199 ± 0.004	
3 (20-2SH53)	RO	0.355 ± 0.002	3.575 ± 0.002	0.800/1.055/1.258
4 (20-2SH16)	FI	0.999 ± 0.002	5.990 ± 0.007	
5 (20-2SH10)	FI	1.000 ± 0.002	7.425 ± 0.007	
6 (20-2SH33)	FI	0.748 ± 0.002	7.639 ± 0.006	
7 (21-2SH02)	RO	0.325 ± 0.002	5.464 ± 0.002	0.803/1.108/1.413
8 (20-2SH58)	RO	0.314 ± 0.003	5.736 ± 0.003	0.761/1.093/1.441
9 (20-2SH63)	RO	0.323 ± 0.002	6.214 ± 0.004	0.805/1.115/1.416
10 (20-2SH62)	RO	0.352 ± 0.003	6.625 ± 0.006	0.799/1.108/1.410

^aFI = front surface impact experiment and RO = release wave overtake experiment.

^bThe listed values have ± 0.002 mm uncertainty.

^cThe listed values are the combined thickness (h_{tar}) of the Ag buffer and Ag sample for each of the three probe locations in the RO experiments.

wave arrival at the Ag/LiF interface for each sample and the measured particle velocity shows an abrupt jump to the peak interface velocity. The velocity then remains constant until the arrival of the release wave from the back of the impactor [marked with arrows in Fig. 3(a)]; as expected, the constant state duration decreases with increasing sample thickness. The measured time interval (Δt) between the shock wave arrival and the release wave arrival is listed for each Ag thickness in Table III.

A release wave overtake experiment (experiment 3) and a front surface impact experiment (experiment 4) were conducted at comparable stresses to demonstrate the good agreement between the sound speeds obtained using the two configurations.

IV. ANALYSIS AND DISCUSSION

A. Determination of Hugoniot states

For experiments using the front surface impact configuration (experiments 1, 2, 4–6), the Ag Hugoniot states—listed in

Table II—were obtained using the measured Ag-LiF interface velocity (u_I), the measured projectile velocity (V_{pr}), and the reported Hugoniot relations for [100] LiF [40] and Ag [34]. For completeness, we note that the Ag Hugoniot is not needed for the stress determination, but is needed for the density determination, in front surface impact experiments.

For experiments using the overtake configuration (experiments 3, 7–10), the impact was symmetric (Ag impactor and Ag sample). Hence, the Ag Hugoniot states were determined directly from the measured impactor velocities, the measured shock velocities, and the Rankine-Hugoniot jump conditions [9,41,42]. The results are listed in Table II. For all of the experiments, including both configurations, the uncertainties shown in Table II were determined using the Monte Carlo method [43] to propagate the uncertainties associated with the measured velocities and with the LiF Hugoniot curve.

Figure 4 shows the measured Hugoniot states (Table II) in the shock velocity (U_s)–particle velocity (u_p) plane and in the stress (P_x)–particle velocity (u_p) plane. U_s values for experiments 1, 2, 4–6 are not shown in Fig. 4(a) because they were

TABLE II. Hugoniot states for shock-compressed Ag.

Expt. No.	Impactor velocity, V_p (mm/ μ s)	Shock velocity, U_s (mm/ μ s)	Ag/LiF interface velocity, u_I (mm/ μ s)	In-material Ag particle velocity, u_p (mm/ μ s)	Longitudinal stress, P_x (GPa)	Density compression, ρ/ρ_0
1	3.822 ± 0.005	5.13 ± 0.05^a	2.64 ± 0.03	1.18 ± 0.03^b	61 ± 1	1.300 ± 0.006^a
2	5.199 ± 0.004	5.80 ± 0.08^a	3.60 ± 0.04	1.60 ± 0.04^b	96 ± 2	1.381 ± 0.009^a
3	3.575 ± 0.002	6.17 ± 0.06	2.49 ± 0.01	1.788 ± 0.001^c	116 ± 1	1.408 ± 0.006
4	5.990 ± 0.007	6.21 ± 0.10^a	4.14 ± 0.05	1.85 ± 0.05^b	118 ± 3	1.425 ± 0.010^a
5	7.425 ± 0.007	6.94 ± 0.13^a	5.12 ± 0.07	2.30 ± 0.07^b	164 ± 4	1.497 ± 0.012^a
6	7.639 ± 0.006	7.06 ± 0.13^a	5.26 ± 0.08	2.38 ± 0.08^b	171 ± 4	1.508 ± 0.012^a
7	5.464 ± 0.002	7.59 ± 0.07	3.83 ± 0.02	2.732 ± 0.001^c	218 ± 2	1.563 ± 0.008
8	5.736 ± 0.003	7.75 ± 0.07	4.02 ± 0.02	2.868 ± 0.002^c	234 ± 2	1.587 ± 0.008
9	6.214 ± 0.004	8.26 ± 0.08	4.34 ± 0.02	3.107 ± 0.002^c	269 ± 3	1.603 ± 0.010
10	6.625 ± 0.006	8.61 ± 0.09	4.62 ± 0.02	3.312 ± 0.003^c	299 ± 3	1.626 ± 0.011

^aDetermined using the Ag Hugoniot curve from Ref. [34].

^bDetermined using $u_p = V_p - u_I$.

^cDetermined using $u_p = V_p/2$.

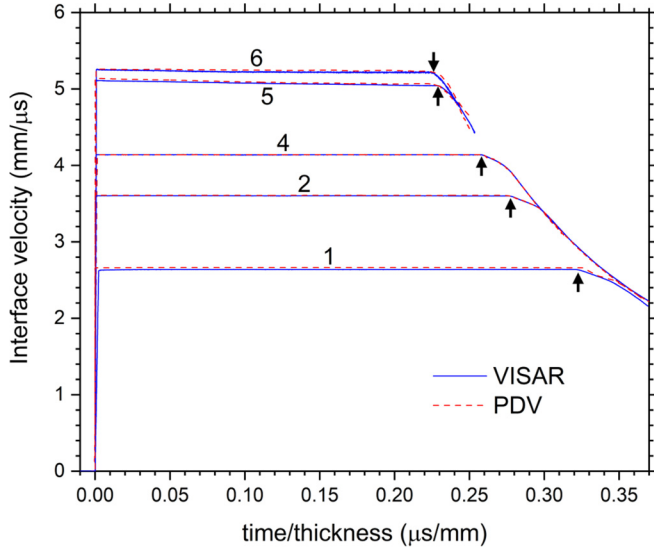


FIG. 2. Measured wave profiles (VISAR and PDV) at the Ag/LiF interface (impact surface) for the front surface impact experiments (experiments 1, 2, 4–6). The time axis is normalized by the Ag impactor thickness. Time zero denotes impact.

not directly measured in the front surface impact experiments. Also shown in Fig. 4 are the Hugoniot curves resulting from the linear U_s-u_p relationship determined previously [34],

$$U_s = (3.21 \pm 0.02 \text{ mm}/\mu\text{s}) + (1.62 \pm 0.02)u_p. \quad (1)$$

As shown in Fig. 4, the Hugoniot states determined in the front surface impact experiments and in the release wave overtake experiments are in very good agreement with each other and with the U_s-u_p relation determined previously [34].

B. Determination of sound speeds and elastic moduli

For the front surface impact configuration (experiments 1, 2, 4–6), the left-going shock wave in the Ag impactor reflects as a release wave from the impactor rear surface, as shown in Fig. 5(a). Thus, the release wave arrival time (Δt) at the

impact surface is given by

$$\Delta t = \frac{h_i}{U_s} + \frac{h_i}{c_L}, \quad (2)$$

where h_i is the impactor thickness (see Table I) and c_L is the Lagrangian release wave speed. Using the Lagrangian sound speed determined from Eq. (2) and accounting for the sample thickness change due to compression, the Eulerian sound speed (or the longitudinal sound speed in the shocked state) can be determined from

$$c_E = c_L \frac{\rho_0}{\rho}, \quad (3)$$

where ρ is density in the shocked Ag. The results are listed in Table III.

For the release wave overtake configuration (experiments 3, 7–10), wave propagation is not as straightforward as the front surface impact configuration. The release wave from the impactor rear surface propagates to the Ag-LiF interface, as shown in Fig. 5(b). In addition, the right-going shock wave reaches the Ag-LiF interface at time t_{sh} and reflects from the LiF window as a release wave. The interaction of the two release waves alters the velocity of the right-going release wave, which reaches the Ag-LiF interface at time t_{rel} . To accurately determine the velocity of the right-going release wave, prior to the interaction with the left-going release wave, the change in velocity caused by the wave interaction must be accounted for. This was accomplished using the following approach, based on the developments pioneered by McQueen, Brown, and co-workers [25,26,39].

In the ideal case, shown in Fig. 5(c), the thickness of the Ag target is such that the right-going shock wave and the right-going release wave reach the Ag-LiF interface at the same time ($t_{rel} = t_{sh}$). In this special case, the Lagrangian sound speed c_L can be determined by solving the following equation:

$$\Delta t = t_{rel} - t_{sh} = \frac{h_i}{U_s} + \frac{h_i}{c_L} + \frac{h_{ov}}{c_L} - \frac{h_{ov}}{U_s} = 0, \quad (4)$$

where h_{ov} is the ideal overtake thickness of the Ag target, h_i is the impactor thickness, and U_s is the shock velocity. Thus, for a given h_i and U_s , determination of the ideal Ag

TABLE III. Sound speeds and Grüneisen parameter for shock-compressed Ag.

Expt. No.	Long. stress, P_x (GPa)	Release wave arrival time, Δt (ns) I/II/III ^a	Ag overtake thickness, h_{ov} (mm)	Eulerian longitudinal sound speed, c_E (mm/ μ s)	Longitudinal modulus, L (GPa)	Grüneisen parameter, Γ	$\rho\Gamma$ (g/cm ³)
1	61 ± 1	114.9		6.07 ± 0.16	503 ± 25		
2	96 ± 2	277.6		6.93 ± 0.19	697 ± 36		
3	116 ± 1	49.2/33.0/15.2	1.478 ± 0.010	7.08 ± 0.06	741 ± 12		
4	118 ± 3	258.4		7.20 ± 0.23	776 ± 45		
5	164 ± 4	229.6		7.82 ± 0.30	962 ± 68		
6	171 ± 4	168.9		7.89 ± 0.31	987 ± 72		
7	218 ± 2	40.1/24.0/6.6	1.537 ± 0.011	7.51 ± 0.08	924 ± 17	1.88 ± 0.14	30.9 ± 2
8	234 ± 2	35.6/17.3/0	1.436 ± 0.024	7.72 ± 0.10	994 ± 24	1.87 ± 0.14	31.2 ± 2
9	269 ± 3	35.7/18.0/2.9	1.464 ± 0.010	8.05 ± 0.09	1092 ± 21	1.75 ± 0.15	29.5 ± 3
10	299 ± 3	39.9/24.1/7.8	1.561 ± 0.012	8.35 ± 0.10	1189 ± 25	1.71 ± 0.15	29.2 ± 3

^aThe listed values have ±0.5-ns uncertainty.

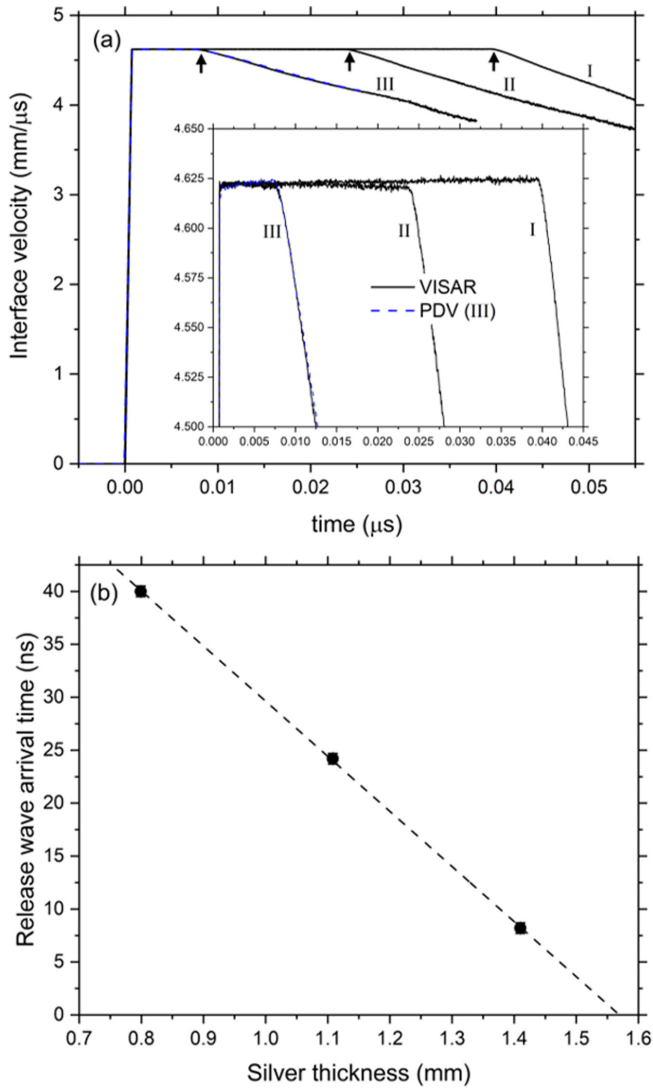


FIG. 3. (a) Wave profiles measured at the Ag/LiF window interface for samples I, II, and III from experiment 10. For each profile, time zero denotes shock wave arrival at the Ag/LiF interface, and release wave arrival is indicated by arrows. (b) Release wave arrival time (Δt) as a function of Ag target thickness for experiment 10. The dashed line shows the best linear fit to the data.

target thickness h_{ov} required to satisfy $\Delta t = t_{rel} - t_{sh} = 0$ is sufficient to determine c_L .

To determine h_{ov} , three wave profile measurements were obtained in each release wave overtake experiment [see Fig. 3(a)], corresponding to Ag targets having three different thicknesses (see Table I). For each measured profile, the difference between the arrival time of the shock wave and that of the release wave ($\Delta t = t_{rel} - t_{sh}$) was measured and is listed in Table III. The three measured Δt values were plotted as a function of Ag target thickness, as shown in Fig. 3(b), and a straight line was fit to the results. Extrapolation of the straight line to $\Delta t = 0$ provides the desired h_{ov} value. Having determined h_{ov} , c_L was determined using Eq. (4), and the Eulerian sound speed c_E , shown in Table III, was determined using Eq. (3).

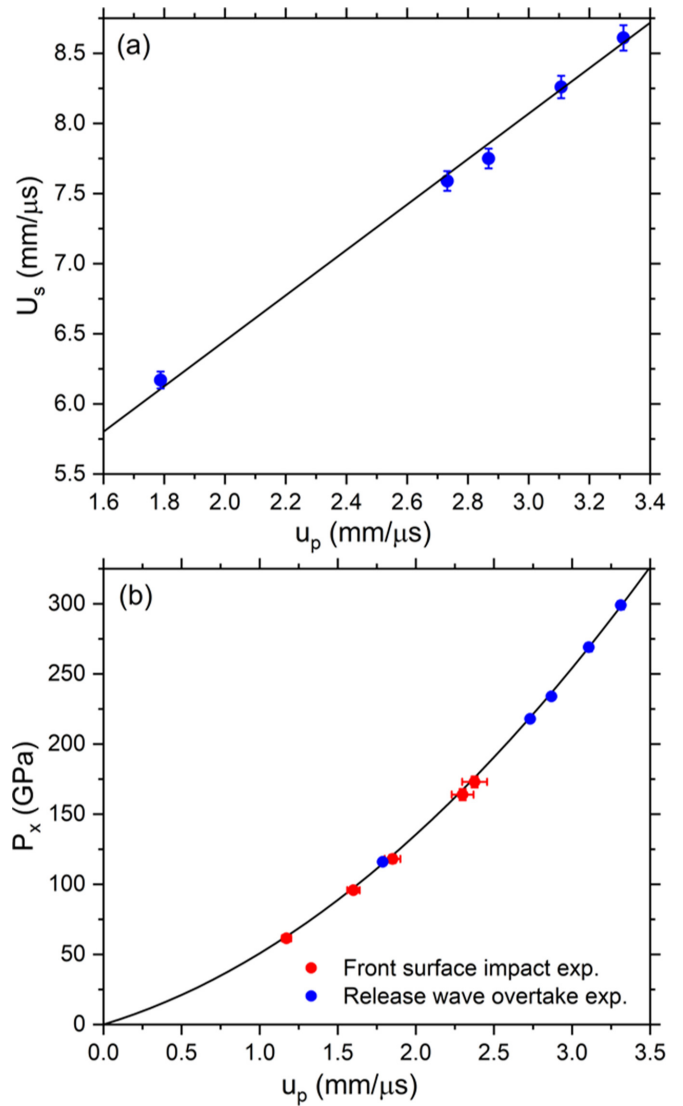


FIG. 4. (a) Shock velocity–particle velocity and (b) longitudinal stress–particle velocity Hugoniot states for shock-compressed Ag from the release wave overtake experiments (blue circles; experiments 3, 7–10). The red circles are the stress–particle velocity states measured in the front surface impact experiments (experiments 1, 2, 4–6). The error bars for the stress–particle velocity states are smaller than the size of the symbols. The black curves were determined from the linear U_s – u_p relation reported previously [34].

Although not explicitly stated/discussed in previous studies [22,25–32,39], the release wave overtake approach is based on the following assumption: details of the wave interaction [Fig. 5(b)] between the right-going release wave in the sample and the left-going reflection from the sample/window interface are independent of the distance traveled by the right-going shock. This assumption is the basis for determining the ideal overtake distance, h_{ov} . The reasonableness of this assumption for the present work is justified by the good agreement between experiments 3 and 4 (~ 117 GPa, utilizing different experimental configurations), the linear fit [Fig. 3(b)] observed for all overtake experiments, and the discussion in the Appendix. For experiments where the wave profiles

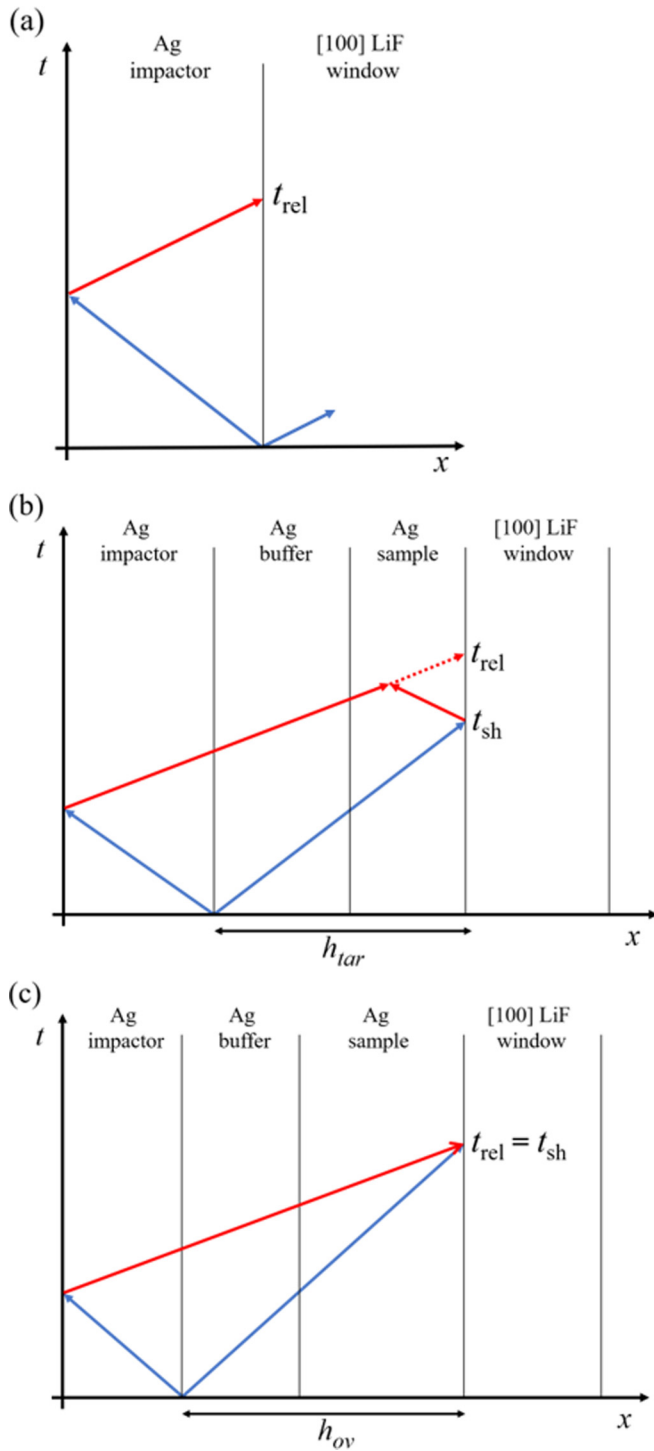


FIG. 5. Time-distance diagrams for (a) front surface impact experiments, (b) release wave overtake experiments, and (c) ideal release wave overtake experiment ($h_{tar} = h_{ov}$). The blue and red arrows represent shock and release waves, respectively. The dashed red arrow represents the release wave propagating through partially released Ag.

display multiple waves or significant changes with propagation distance, the validity of this assumption may be questionable.

The Eulerian sound speeds, listed in Table III, are plotted as functions of stress and density compression in Fig. 6. The

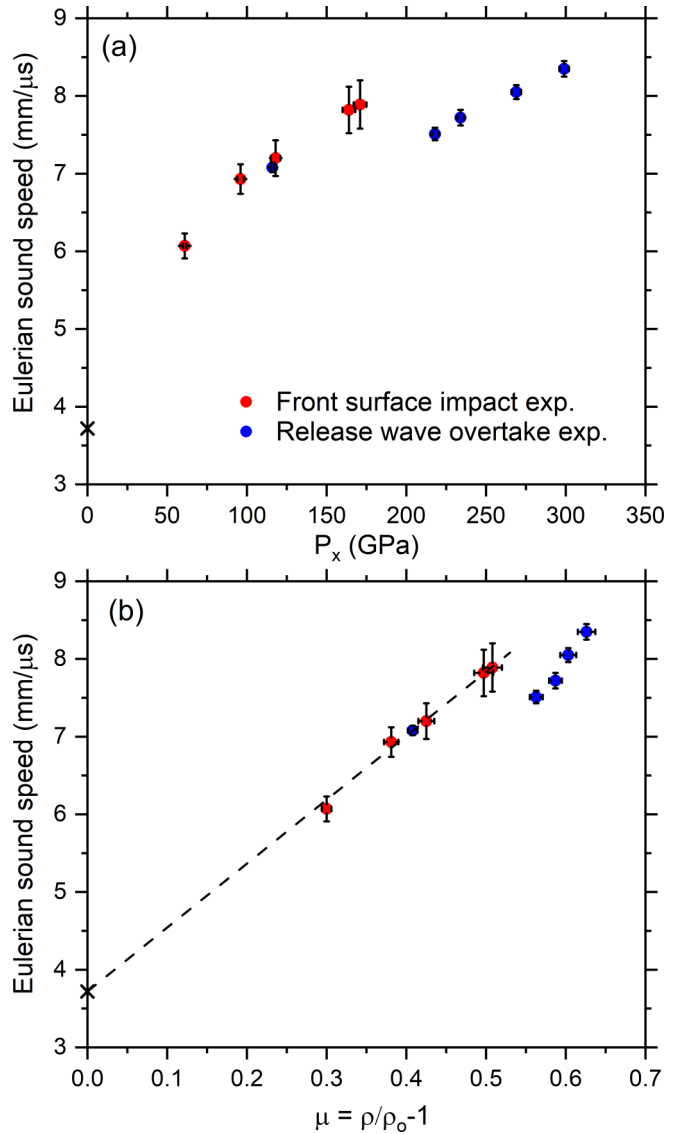


FIG. 6. The Eulerian longitudinal sound speed as a function of stress (a) and density compression (b) in shock-compressed Ag. The black X denotes the ambient longitudinal sound speed. The dashed line is a linear fit to the sound speeds for $\mu < 0.51$ [see Eq. (6)].

sound speeds increase strongly and smoothly up to 171 GPa [Fig. 6(a)]; in terms of density compression, the increase is linear up to 50% compression. At 218 GPa (56% compression), there is a significant reduction in the sound speed before increasing again at higher stresses. As an aside, we note that the sound speed data in Fig. 6(b) are well matched to a linear fit to 50% compression.

The isentropic longitudinal elastic moduli in the shocked state can be determined from the Eulerian sound speeds using

$$L = \rho c_E^2. \quad (5)$$

These results are shown in Fig. 7 and listed in Table III. The elastic modulus at ~ 170 GPa—despite the temperature increase due to shock compression—is more than five times the ambient value and demonstrates the increasing incompressibility with compression.

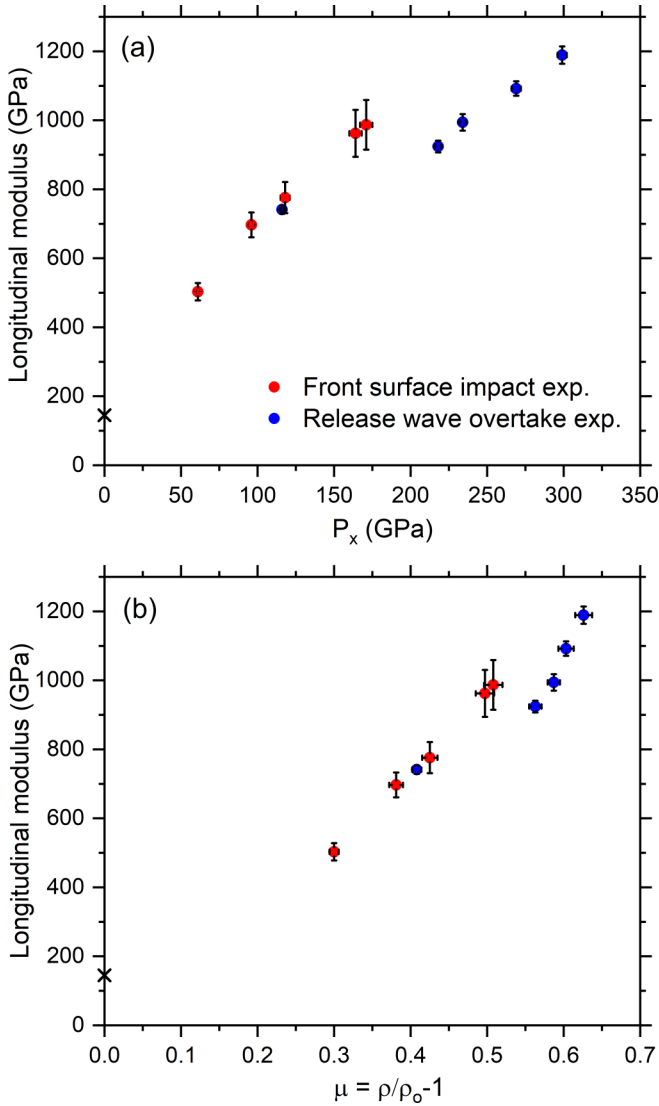


FIG. 7. Longitudinal isentropic elastic modulus as a function of stress (a) and density compression (b) in shock-compressed Ag. The black X denotes the ambient longitudinal isentropic elastic modulus.

C. Discussion

As noted earlier, the x-ray diffraction data on shock-compressed Ag [16] have established the occurrence of a solid-solid transformation at ~ 150 GPa and the onset of melting between 172 and 197 GPa. Furthermore, a detailed examination of the measured wave profiles provided the following results [34]: the onset of melting occurs between 172 and 187 GPa, the solid-liquid mixed phase occurs between 187 and 210 GPa, and Ag is in a liquid state above 210 GPa. Recent theoretical determinations of the Ag phase diagram [23,24], motivated by the previous experimental results [16,34], are consistent with the experimentally determined transition stresses for the solid-solid and solid-liquid transformations. The results in Figs. 6 and 7 complement the earlier results [16,34] and provide further insights into the shock compressed state of Ag, as discussed below.

The measured sound speed and longitudinal moduli show no discontinuity or change in slope due to the fcc-bcc phase

transition at ~ 150 GPa. The sound speed data in solid Ag [Fig. 6(b)] to $\sim 50\%$ compression (171 GPa) can be fitted as follows:

$$c_E = 3.72 + 8.22 \left(\frac{\rho}{\rho_0} - 1 \right) \text{ mm}/\mu\text{s}. \quad (6)$$

Thus, our results—within experimental uncertainties—show that the longitudinal moduli in the fcc and bcc phases are well matched. Whether the similarity in longitudinal moduli ($B + 4/3 G$) will hold for bulk (B) and shear (G) moduli, separately, across the fcc-bcc phase change cannot be ascertained from our results.

The drop in the sound speed and the longitudinal modulus at 218 GPa suggests that melting is complete at 218 GPa, a finding consistent with XRD results [16] and recent wave profile measurements [34].

Perhaps, the optimal validation of the Ag liquid response above 218 GPa can be ascertained by considering the requirement for the propagation of a stable shock in a liquid [44,45]: the isentrope in the shocked state (the longitudinal modulus) should lie between the Hugoniot and the Rayleigh line. All the results (Figs. 6 and 7) at and above 218 GPa satisfy this requirement.

In the liquid phase, the measured sound speeds—together with the Ag Hugoniot curve—can be used to determine the Grüneisen parameter (Γ) by solving [9]

$$\rho B = \rho^2 c_E^2 = -\frac{dP_H}{dV} \left[1 - \frac{\Gamma}{V} \frac{(V_0 - V)}{2} \right] + \frac{\Gamma}{V} \frac{P_H}{2}, \quad (7)$$

where $V = 1/\rho$ is specific volume, P_H is pressure on the Hugoniot curve for liquid Ag, and dP_H/dV is the derivative along the Hugoniot. The Grüneisen parameter values for liquid Ag determined using Eq. (7) are listed in Table III; these values are significantly smaller than the ambient value ($\Gamma = 2.49$) determined from published thermodynamic data [34,46] using [47]

$$\Gamma = \frac{\beta B}{\rho C_P}, \quad (8)$$

where β is the volume thermal expansion coefficient and C_P is the specific heat at constant pressure.

For metals shock compressed to high stresses, it is commonly assumed that the density–Grüneisen parameter product $\rho\Gamma$ is constant [9,42]. Within experimental uncertainty, the measured $\rho\Gamma$ values, shown in Table III and in Fig. 8, are the same (average value, $30.2 \text{ g}/\text{cm}^3$), showing that $\rho\Gamma$ is constant in the liquid phase up to ~ 300 GPa. However, the measured $\rho\Gamma$ values for liquid Ag differ from the ambient value ($\rho\Gamma = 26.1 \text{ g}/\text{cm}^3$) for solid Ag (dashed line in Fig. 8). Given the constancy of $\rho\Gamma$, the $E(P,V)$ EOS for liquid Ag can be written as

$$P = P_H \left[1 - \frac{\Gamma}{2} \left(\frac{V_0}{V} - 1 \right) \right] + \rho\Gamma E. \quad (9)$$

The above $E(P,V)$ EOS can be used to calculate off-Hugoniot states, including isentropes and multishocked states. To calculate temperatures, determination of specific heat at constant volume (C_V) is required.

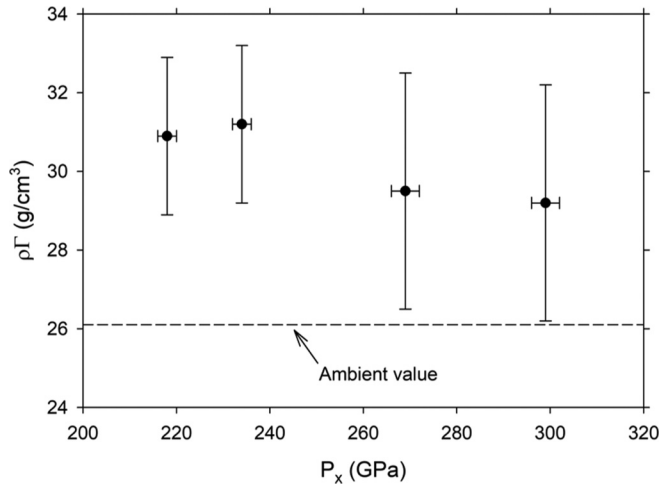


FIG. 8. Density–Grüneisen parameter product ($\rho\Gamma$) as a function of stress. The dashed line shows the $\rho\Gamma$ value at ambient conditions.

V. SUMMARY AND CONCLUSIONS

Wave profiles were measured using laser interferometry to determine longitudinal sound speeds and Hugoniot states in Ag shock compressed to peak stresses between 60 and 300 GPa. The sound speed results presented here complement previous XRD results [16] and wave profile measurements [34] on shock-compressed Ag, providing additional insight into the fcc-to-bcc transformation and melting reported previously [16]. The main findings from this work are as follows:

(i) The measured sound speed and longitudinal moduli show no discontinuity or change in slope due to the fcc-bcc phase transition at ~ 150 GPa; the sound speed data in solid Ag [Fig. 6(b)] are well fit by a straight line up to $\sim 50\%$ compression (171 GPa). These results show that, within experimental uncertainty, the sound speeds and longitudinal elastic moduli are well matched in the fcc and bcc phases.

(ii) The significant drop in sound speed observed between 171 and 218 GPa suggests that melting in shock-compressed Ag is complete at 218 GPa. This finding is consistent with XRD results [16] and wave profile measurements [34] reported previously.

(iii) The Grüneisen parameter Γ for liquid Ag was determined at stresses up to ~ 300 GPa. Within experimental uncertainty, the $\rho\Gamma$ product, often assumed constant for shock compressed metals [9,42], was shown to be indeed constant for liquid Ag from 218 to ~ 300 GPa. However, the $\rho\Gamma$ product for liquid Ag differs from that for solid Ag determined at ambient conditions.

The results presented here provide important insight into the response of Ag shock compressed into the liquid phase—insight not obtainable from the recent XRD measurements [16]. In particular, the present sound speed measurements provide key thermodynamic constraints to guide EOS developments for liquid Ag at multimegabar stresses. Determination of the constant $\rho\Gamma$ product establishes the $E(P,V)$ EOS for liquid Ag, which can be used to calculate off-Hugoniot states. However, determination of temperature requires a complete $E(S,V)$ EOS that incorporates a description of the specific heat (C_V).

ACKNOWLEDGMENTS

N. Arganbright, Y. Toyoda, and K. Zimmerman are gratefully acknowledged for their expert assistance with the experiments. This work was supported by the U.S. Department of Energy (DOE), National Nuclear Security Administration (NNSA) under Cooperative Agreement No. DE-NA0003957.

APPENDIX: JUSTIFICATION FOR USING THE RELEASE WAVE OVERTAKE METHOD

As discussed in Sec. IV B, the release wave overtake approach is based on the following assumption: details of the wave interaction [Fig. 5(b)] between the right-going release wave in the sample and the left-going reflection from the sample/window interface are independent of the distance traveled by the right-going shock. For the present results, the shock propagates as a steady single wave. Therefore, the above assumption is valid if the right-going release wave in the sample and the left-going reflection both propagate as centered simple waves because, in that case, the propagation of each wave—prior to their interaction—is self-similar and the flow variables do not depend on distance (x) and time (t) independently, but only on the combination x/t [48,49]. Such is clearly the case for Ag released from the liquid state (experiments 7–10; Fig. 3), where the release path is along an isentrope [9,49].

For Ag released from the solid state (experiment 3), the release path involves the Ag elastic-plastic response. To determine the validity of the release wave overtake method for materials that exhibit time-independent elastic-plastic release

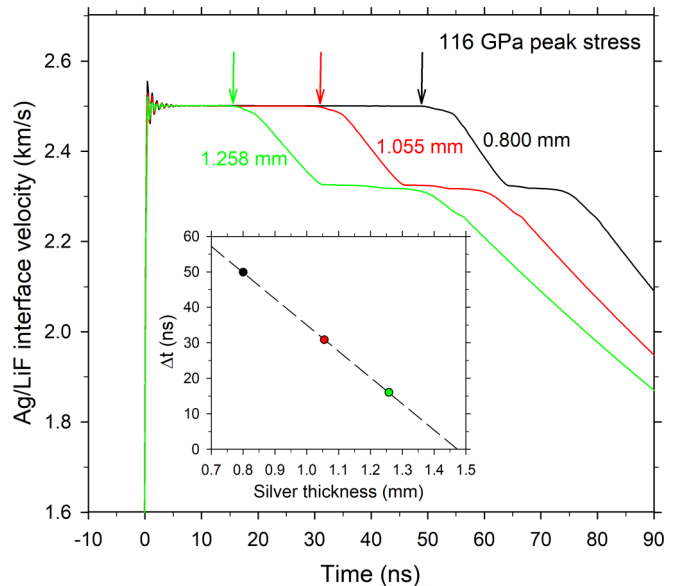


FIG. 9. Wave profiles at the Ag/LiF window interface calculated using the configuration from experiment 3. Each profile corresponds to the sample thickness indicated; time zero denotes shock wave arrival at the Ag/LiF interface; and release wave arrival is indicated by arrows. The inset shows the calculated release wave arrival times (Δt) as a function of Ag target thickness. The dashed line shows the best linear fit to the calculated results.

response, we carried out numerical simulations using the experimental configuration for experiment 3 [Fig. 1(b)].

The Ag material model used in the calculations incorporates the linear U_s-u_p relationship from Eq. (1), together with the assumption that $\rho\Gamma$ is constant, to determine the mean stress response. For the deviatoric stress response, the shear modulus was assumed to have a linear dependence on the mean stress

$$G = G_0 + G_1P, \quad (\text{A1})$$

and shear strength was described using a time-independent strain-hardening model,

$$Y = Y_0 + M\bar{\epsilon}_p. \quad (\text{A2})$$

In Eq. (A2), $\bar{\epsilon}_p$ is the effective plastic strain, M is the strain-hardening modulus, and Y_0 is the yield stress at the elastic limit.

The calculated wave profiles for the three sample thicknesses from experiment 3 (Table I) are shown in Fig. 9. For

each profile, time zero corresponds to the shock wave arrival at the Ag/LiF interface; the arrival of the release wave from the back of the impactor is marked with arrows. The focus of the simulations was on the release wave arrival and not on the subsequent wave profile structure.

Figure 9 inset shows the calculated time interval (Δt) between the shock wave arrival and the release wave arrival plotted against Ag sample thickness. As with the measured results, the calculated Δt values are well fit by a straight line. Extrapolation of the straight line to $\Delta t = 0$ provides the calculated ideal overtake thickness, $h_{ov} = 1.471$ mm. Using h_{ov} , together with the calculated shock velocity and density compression in Eqs. (3) and (4) yields the calculated Eulerian sound speed, $c_E = 7.116$ mm/ μ s. For comparison, the Eulerian sound speed determined directly from the propagation of the release wave in the simulations yields $c_E = 7.102$ mm/ μ s, which differs from the above release wave overtake result by less than 0.2%. Therefore, the numerical simulations presented here show that the release wave overtake method provides an accurate sound speed determination for materials, such as Ag, having a time-independent elastic-plastic release response.

-
- [1] D. L. Heinz and R. Jeanloz, The equation of state of the gold calibration standard, *J. Appl. Phys.* **55**, 885 (1984).
- [2] N. C. Holmes, J. A. Moriarty, G. R. Gathers, and W. J. Nellis, The equation of state of platinum to 660 GPa (6.6 Mbar), *J. Appl. Phys.* **66**, 2962 (1989).
- [3] Y. Akahama, H. Kawamura, and A. K. Singh, A comparison of volume compressions of silver and gold up to 150 GPa, *J. Appl. Phys.* **95**, 4767 (2004).
- [4] A. Dewaele, P. Loubeyre, and M. Mezouar, Equations of state of six metals above 94 GPa, *Phys. Rev. B* **70**, 094112 (2004).
- [5] A. Dewaele, M. Torrent, P. Loubeyre, and M. Mezouar, Compression curves of transition metals in the Mbar range: Experiments and projector augmented-wave calculations, *Phys. Rev. B* **78**, 104102 (2008).
- [6] K. Takemura and A. Dewaele, Isothermal equation of state for gold with a He-pressure medium, *Phys. Rev. B* **78**, 104119 (2008).
- [7] M. Yokoo, N. Kawai, K. G. Nakamura, K. I. Kondo, Y. Tange, and T. Tsuchiya, Ultrahigh-pressure scales for gold and platinum at pressures up to 550 GPa, *Phys. Rev. B* **80**, 104114 (2009).
- [8] A. Dewaele, P. Loubeyre, F. Occelli, O. Marie, and M. Mezouar, Toroidal diamond anvil cell for detailed measurements under extreme static pressures, *Nat. Commun.* **9**, 2913 (2018).
- [9] R. G. McQueen, S. P. Marsh, J. W. Taylor, J. N. Fritz, and W. J. Carter, in *High-Velocity Impact Phenomena*, edited by R. Kinslow (Academic, New York, 1970), pp. 293–417.
- [10] *LASL Shock Hugoniot Data*, edited by S. P. Marsh (University of California Press, Los Angeles, 1980).
- [11] A. C. Mitchell and W. J. Nellis, Shock compression of aluminum, copper, and tantalum, *J. Appl. Phys.* **52**, 3363 (1981).
- [12] C. W. Greeff and M. J. Graf, Lattice dynamics and the high-pressure equation of state of Au, *Phys. Rev. B* **69**, 054107 (2004).
- [13] C. W. Greeff, J. C. Boettger, M. J. Graf, and J. D. Johnson, Theoretical investigation of the Cu EOS standard, *J. Phys. Chem. Solids* **67**, 2033 (2006).
- [14] S. M. Sharma, S. J. Turneaure, J. M. Winey, Y. Li, P. Rigg, A. Schuman, N. Sinclair, Y. Toyoda, X. Wang, N. Weir, J. Zhang, and Y. M. Gupta, Structural Transformation and Melting in Gold Shock Compressed to 355 GPa, *Phys. Rev. Lett.* **123**, 045702 (2019).
- [15] R. Briggs, F. Coppari, M. G. Gorman, R. F. Smith, S. J. Tracy, A. L. Coleman, and A. Fernandez-Pañella, Measurement of Body-Centered Cubic Gold and Melting under Shock Compression, *Phys. Rev. Lett.* **123**, 045701 (2019).
- [16] S. M. Sharma, S. J. Turneaure, J. M. Winey, and Y. M. Gupta, What Determines the fcc-bcc Structural Transformation in Shock Compressed Noble Metals?, *Phys. Rev. Lett.* **124**, 235701 (2020).
- [17] S. M. Sharma, S. J. Turneaure, J. M. Winey, and Y. M. Gupta, Transformation of shock compressed copper to the body centered cubic structure at 180 GPa, *Phys. Rev. B* **102**, 020103(R) (2020).
- [18] N. R. Mitra, D. L. Decker, and H. B. Vanfleet, Melting curves of copper, silver, gold, and platinum to 70 kbar, *Phys. Rev.* **161**, 613 (1967).
- [19] D. Errandonea, The melting curve of ten metals up to 12 GPa and 1600 K, *J. Appl. Phys.* **108**, 033517 (2010).
- [20] H. Brand, D. P. Dobson, L. Vočadlo, and I. G. Wood, Melting curve of copper measured to 16 GPa using a multi-anvil press, *High Press. Res.* **26**, 185 (2006).
- [21] S. Japel, B. Schwager, R. Boehler, and M. Ross, Melting of Copper and Nickel at High Pressure: The Role of d Electrons, *Phys. Rev. Lett.* **95**, 167801 (2005).
- [22] D. Hayes, R. S. Hixson, and R. G. McQueen, in *Shock Compression of Condensed Matter - 1999*, edited by M. D. Furnish, L. C. Chhabildas, and R. S. Hixson (American Institute of Physics, New York, 2000), p. 483.

- [23] N. A. Smirnov, Relative stability of Cu, Ag, and Pt at high pressures and temperatures from *ab initio* calculations, *Phys. Rev. B* **103**, 064107 (2021).
- [24] S. R. Baty, L. Burakovsky, and D. Errandonea, *Ab initio* phase diagram of silver, *J. Phys.: Condens. Matter* **33**, 485901 (2021).
- [25] J. M. Brown and R. G. McQueen, Melting of iron under core conditions, *Geophys. Res. Lett.* **7**, 533 (1980).
- [26] J. M. Brown and R. G. McQueen, Phase transitions, Grüneisen parameter, and elasticity for shocked iron between 77 GPa and 400 GPa, *J. Geophys. Res.* **91**, 7485 (1986).
- [27] R. S. Hixson, D. A. Boness, J. W. Shaner, and J. A. Moriarty, Acoustic Velocities and Phase Transitions in Molybdenum under Strong Shock Compression, *Phys. Rev. Lett.* **62**, 637 (1989).
- [28] J. H. Nguyen and N. C. Holmes, Melting of iron at the physical conditions of the Earth's core, *Nature (London)* **427**, 339 (2004).
- [29] J. H. Nguyen, M. C. Akin, R. Chau, D. E. Fratanduono, W. P. Ambrose, O. V. Fat'yanov, P. D. Asimow, and N. C. Holmes, Molybdenum sound velocity and shear modulus softening under shock compression, *Phys. Rev. B* **89**, 174109 (2014).
- [30] C. A. McCoy, M. D. Knudson, and S. Root, Absolute measurement of the Hugoniot and sound velocity of liquid copper at multimegabar pressures, *Phys. Rev. B* **96**, 174109 (2017).
- [31] M. C. Akin, J. H. Nguyen, M. A. Beckwith, R. Chau, W. P. Ambrose, O. V. Fat'yanov, P. D. Asimow, and N. C. Holmes, Tantalum sound velocity under shock compression, *J. Appl. Phys.* **125**, 145903 (2019).
- [32] C. A. McCoy, M. D. Knudson, and M. P. Desjarlais, Sound velocity, shear modulus, and shock melting of beryllium along the Hugoniot, *Phys. Rev. B* **100**, 054107 (2019).
- [33] A. V. Altshuler, A. A. Bakanova, I. P. Dudoladov, E. A. Dynin, R. F. Trunin, and B. S. Chekin, Shock adiabatic curves of metals. New data, statistical analysis, and general laws, *J. Appl. Mech. Tech. Phys.* **22**, 145 (1981).
- [34] M. K. Wallace, J. M. Winey, and Y. M. Gupta, Shock compression of silver to 300 GPa: Wave profile measurements and melting transition, *Phys. Rev. B* **104**, 014101 (2021).
- [35] G. Simmons and H. Wang, *Single Crystal Elastic Constants and Calculated Aggregate Properties: A Handbook* (MIT Press, Cambridge, 1971).
- [36] E. B. Zaretsky and G. I. Kanel, Plastic flow in shock-loaded silver at strain rates from 10^4 s^{-1} to 10^7 s^{-1} and temperatures from 296 K to 1233 K, *J. Appl. Phys.* **110**, 073502 (2011).
- [37] L. M. Barker and R. E. Hollenbach, Laser interferometer for measuring high velocities of any reflecting surface, *J. Appl. Phys.* **43**, 4669 (1972).
- [38] O. T. Strand, D. R. Goosman, C. Martinez, T. L. Whitworth, and W. W. Kuhlow, Compact system for high-speed velocimetry using heterodyne techniques, *Rev. Sci. Instrum.* **77**, 083108 (2006).
- [39] R. G. McQueen, J. W. Hopson, and J. N. Fritz, Optical technique for determining rarefaction wave velocities at very high pressures, *Rev. Sci. Instrum.* **53**, 245 (1982).
- [40] P. A. Rigg, M. D. Knudson, R. J. Scharff, and R. S. Hixson, Determining the refractive index of shocked [100]lithium fluoride to the limit of transmissibility, *J. Appl. Phys.* **116**, 033515 (2014).
- [41] J. M. Walsh, M. H. Rice, R. G. McQueen, and F. L. Yarger, Shock-wave compressions of twenty-seven metals. Equations of state of metals, *Phys. Rev.* **108**, 196 (1957).
- [42] R. G. McQueen and S. P. Marsh, Equation of state for nineteen metallic elements from shock-wave measurements to two megabars, *J. Appl. Phys.* **31**, 1253 (1960).
- [43] Joint Committee for Guides in Metrology, Evaluation of Measurement Data – Supplement 1 to the Guide to the Expression of Uncertainty in Measurement – Propagation of Distributions using a Monte Carlo Method, *JCGM* **101**, 1 (2008).
- [44] R. Courant and K. O. Friedrichs, *Supersonic Flow and Shock Waves*, 1st ed. (Interscience Publishers, New York, 1948); reprint by Springer-Verlag, 1976, Chap. III, Sec. 65.
- [45] Y. B. Zel'dovich and Y. P. Raizer, *Physics of Shock Waves and High-Temperature Hydrodynamic Phenomena*, (Academic, New York, 1966); reprint by Dover, 2002, Chap. I, Sec. 18.
- [46] *American Institute of Physics Handbook*, edited by D. E. Gray (McGraw-Hill, New York, 1972).
- [47] D. C. Wallace, *Thermodynamics of Crystals* (Wiley, New York, 1972).
- [48] R. Courant and K. O. Friedrichs, *Supersonic Flow and Shock Waves*, 1st ed. (Interscience Publishers, New York, 1948); reprint by Springer-Verlag, 1976, Chap. III, Sec. 46.
- [49] Y. B. Zel'dovich and Y. P. Raizer, *Physics of Shock Waves and High-Temperature Hydrodynamic Phenomena*, (Academic, New York, 1966); reprint by Dover, 2002, Chap. I, Sec. 11.